# 4

# Quantum Monte Carlo Study of Anderson Magnetic Impurities in Semiconductors

N. Bulut[1,2], Y. Tomoda[1], K. Tanikawa[1], S. Takahashi[1], and S. Maekawa[1,2]

[1] Institute for Materials Research, Tohoku University, Sendai 980-8577, Japan
[2] CREST, Japan Science and Technology Agency (JST), Kawaguchi, Saitama 332-0012, Japan, nbulut@imr.tohoku.ac.jp, tomoyoshi@imr.tohoku.ac.jp, tanikawa@imr.tohoku.ac.jp, takahasi@imr.tohoku.ac.jp, maekawa@imr.tohoku.ac.jp

**Summary.** We use quantum Monte Carlo simulations to study the electronic properties of Anderson magnetic impurities in a semiconductor host. We find that in a semiconductor the magnetic impurities exhibit ferromagnetic correlations, which can have a much longer range than in a metallic host. In particular, the range is longest when the Fermi level is located between the top of the valence band and the impurity bound state. We study the dependence of the ferromagnetic correlations on the parameters of the Anderson model, and the dimensionality and band structure of the host material. Using the tight-binding approximation for calculating the host band structure and the impurity–host hybridization, we obtain an impurity bound state, which is located at ≈100 meV above the top of the valence band, which is in agreement with the transport measurements on GaAs with dilute Mn impurities.

## 4.1 Introduction

The discovery of ferromagnetism in alloys of III–V semiconductors with Mn started an intense research activity in the field of dilute magnetic semiconductors (DMS) [1–3]. Within this context, it is important to understand the nature of the correlations that develop between magnetic impurities in semiconductors and how they differ from that in a metallic host. With this purpose, we present Quantum Monte Carlo (QMC) results on the two-impurity Anderson model for a semiconductor host.

The Anderson model of magnetic impurities in a semiconductor host was previously studied using the Hartree-Fock (HF) approximation [4–6] and perturbative techniques [7]. It was shown that long-range ferromagnetic (FM) correlations develop between Anderson impurities in a semiconductor when the Fermi level is located between the top of the valence band and the impurity bound state (IBS) [5, 6], as illustrated in Fig. 4.1.

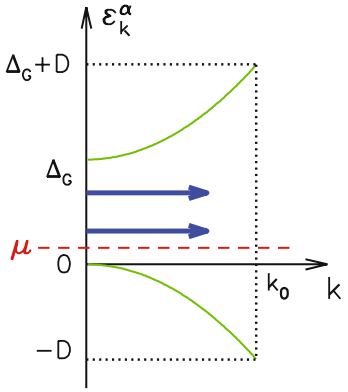


**Fig. 4.1.** Semiconductor host bands $\varepsilon_k^\alpha$ (*solid curves*) and the impurity bound states (*thick arrows*) obtained with HF in the semiconductor gap. The *dashed line* denotes the chemical potential $\mu$

To study the multiple charge states of Au impurities in Ge, the single-impurity Anderson model of a metallic host was extended to the case of a semiconductor host using the HF approximation [4]. After the discovery of DMS, the magnetic properties of this model were addressed within HF [5, 6], and it was shown that long-range FM correlations develop when the Fermi level is located between the top of the valence band and the IBS. The FM interaction between the impurities is mediated by the impurity-induced polarization of the valence electron spins, which are antiferromagnetically coupled to the impurity moments. The impurity-host hybridization also induces host split-off states at the same energy as the IBS. When the split-off state becomes occupied, the spin polarizations of the valence band and of the split-off state cancel. This causes the long-range FM correlations between the impurities to vanish. Within the context of DMS, the Anderson Hamiltonian for a semiconductor host was also considered by Krstajić et al. [7], and it was shown that an FM interaction is generated between the impurities because of kinematic exchange. In addition, this model was studied within HF for investigating the multiple charge and spin states of transition-metal atoms in hemoprotein [8]. Finally, the role of IBS in producing the FM interaction in DMS was also discussed within the "double resonance mechanism" using HF [9].

In this chapter, we present QMC results for the impurity–impurity and impurity–host magnetic correlations in the Anderson model for semiconductor and metallic hosts [10]. We found that, in a semiconductor host, the magnetic correlations do not exhibit Ruderman-Kittel-Kasuya-Yosida (RKKY) type oscillations. Instead, the impurity–impurity magnetic correlations are ferromagnetic with a range that can become strongly enhanced depending on the occupation of IBS. In agreement with the HF results [5, 6], the range is longest when the chemical potential is between the top of the valence band and the IBS. We also show that the FM correlations between the impurities

is generated by the antiferromagnetic (AFM) impurity–host coupling. Comparisons with the experiments on GaAs with dilute Mn impurities suggest that the physical picture presented here describes how magnetic correlations develop between dilute magnetic impurities in a semiconductor host.

In addition, we determine the dependence of the FM correlations between the impurities on the parameters of the Anderson model. We also study the dependence of the FM correlations on the dimensionality and band structure of the host materials. In particular, we use the tight-binding approximation to calculate the host band structure and the impurity–host hybridization, and then use these as input for QMC simulations of the Anderson model. This way of combining the tight-binding approximation with the QMC technique allows us to study the material dependence of the magnetic and electronic properties. For instance, this approach yields an IBS energy of $\approx 100\, meV$, which is comparable to the experimental value. We think that these results are useful for understanding the properties of the DMS and dilute oxide ferromagnets.

In Sect. 4.2, we introduce the Anderson model for a semiconductor host and describe the quantities, which we calculate with QMC, and the parameter regime, which we explore in the simulations. In Sect. 4.3, we show QMC results on the impurity–impurity and impurity–host correlations for the two-dimensional host with a quadratic quasiparticle dispersion. Section 4.4 shows results for the 3D case, while in Sect. 4.5 the QMC results for a magnetic impurity in a GaAs host are discussed using the tight-binding approximation for the band-structure of the host material. Finally, Sect. 4.6 presents a discussion and summary of the numerical results.

## 4.2 Model

The two-impurity Anderson model for a semiconductor host is defined by

$$H = \sum_{\mathbf{k},\alpha,\sigma} (\varepsilon_{\mathbf{k}}^{\alpha} - \mu) c_{\mathbf{k}\alpha\sigma}^{\dagger} c_{\mathbf{k}\alpha\sigma} + \sum_{\mathbf{k},i,\alpha,\sigma} (V_{\mathbf{k}i} c_{\mathbf{k}\alpha\sigma}^{\dagger} d_{i\sigma} + \text{H.c.}) + (E_d - \mu) \sum_{i,\sigma} d_{i\sigma}^{\dagger} d_{i\sigma} + U \sum_{i} d_{i\uparrow}^{\dagger} d_{i\uparrow} d_{i\downarrow}^{\dagger} d_{i\downarrow}, \tag{4.1}$$

where $c_{\mathbf{k}\alpha\sigma}^{\dagger}$ ($c_{\mathbf{k}\alpha\sigma}$) creates (annihilates) a host electron with wavevector $\mathbf{k}$ and spin $\sigma$ in the valence ($\alpha = v$) or conduction ($\alpha = c$) band, and $d_{i\sigma}^{\dagger}$ ($d_{i\sigma}$) is the creation (annihilation) operator for a localized electron at impurity site $i$. The hybridization matrix element is

$$V_{\mathbf{k}j} = V e^{i\mathbf{k}\cdot\mathbf{R}_j}, \tag{4.2}$$

where $\mathbf{R}_j$ is the coordinate of the impurity site $j$. As usual, $E_d$ is the $d$-level energy, $U$ is the onsite Coulomb repulsion, and $\mu$ the chemical potential. In Sects. 4.3 and 4.4, we will use quadratic dispersion for the valence and conduction bands

$$\varepsilon^{v}_{\mathbf{k}} = -D\,(k/k_0)^2 \tag{4.3}$$

$$\varepsilon^{c}_{\mathbf{k}} = D\,(k/k_0)^2 + \Delta_G, \tag{4.4}$$

with $D$ the bandwidth, $k_0$ the maximum wavevector, and $\Delta_{\mathrm{G}}$ the semiconductor gap. In Sect. 4.3, we consider a two-dimensional (2D) semiconductor host with a constant density of states $\rho_0$, and in Sect. 4.4, the three-dimensional (3D) case. Here, the energy scale is determined by setting $D = 12.0$. In Sect. 4.5, we use the tight-binding approximation to calculate the host band structure. In addition, in these calculations we use $U = 4.0$ and $E_d = \mu - U/2$, so that the impurity sites develop large moments both in the metallic and semiconductor cases. We report results for $\Delta_G = 2.0$, and inverse temperature $\beta \equiv 1/T$ from 4 to 32 for the 2D and 3D cases.

The numerical results presented here were obtained with the Hirsch-Fye QMC technique [11]. In the following, we show results on the equal-time impurity–impurity magnetic correlation function $\langle M_1^z M_2^z \rangle$, where the impurity magnetization operator is

$$M_i^z = d_{i\uparrow}^{\dagger} d_{i\uparrow} - d_{i\downarrow}^{\dagger} d_{i\downarrow}, \tag{4.5}$$

for the two-impurity Anderson Hamiltonian, (4.1). In addition, we will discuss the results on the impurity–host correlation function $\langle M^z m^z(r) \rangle$ for the single-impurity Anderson model. Here, the host magnetization at a distance $r$ away from the impurity site is given by

$$m^z(r) = \sum_{\alpha=v,c} (c_{\alpha\uparrow}^{\dagger}(r) c_{\alpha\uparrow}(r) - c_{\alpha\downarrow}^{\dagger}(r) c_{\alpha\downarrow}(r)). \tag{4.6}$$

For the metallic case, $\langle M_1^z M_2^z \rangle$ and $\langle M^z m^z(r) \rangle$ were previously studied by using QMC [11–14].

We also present results on the impurity single-particle spectral weight $A(\omega) = -(1/\pi)\mathrm{Im}\, G_{ii}^{\sigma}(\omega)$, which is obtained with the maximum-entropy analytic continuation technique [15] from the QMC data on the impurity Green's function

$$G_{ii}^{\sigma}(\tau) = -\langle T_\tau\, d_{i\sigma}(\tau) d_{i\sigma}^{\dagger}(0) \rangle. \tag{4.7}$$

Here, $T_\tau$ is the Matsubara time-ordering operator and $d_{i\sigma}(\tau) = \mathrm{e}^{H\tau} d_{i\sigma} \mathrm{e}^{-H\tau}$. Since the maximum-entropy procedure requires QMC data with very good statistics, our results on $A(\omega)$ will be limited to the high-temperature $\beta = 8$ case. In addition, we present data on the zero-frequency inter-impurity magnetic susceptibility defined by

$$\chi_{12} = \int_0^{\beta} \mathrm{d}\tau \langle M_1^z(\tau) M_2^z(0) \rangle \tag{4.8}$$

for the two-impurity case. The following results were obtained using Matsubara time step $\Delta\tau = 0.25$ except for $A(\omega)$ which was obtained with $\Delta\tau = 0.125$.

At $\beta = 16$, $\langle M_1^z M_2^z \rangle$ varies by a few percent as $\Delta\tau$ decreases from 0.25 to 0.125.

For the single-impurity Anderson model, we present QMC data on the square of the impurity moment, $\langle (M^z)^2 \rangle$, and the impurity susceptibility $\chi$ defined by

$$\chi = \int_0^\beta \mathrm{d}\tau \langle M^z(\tau) M^z(0) \rangle. \tag{4.9}$$

The effects of IBS are clearly visible in these quantities. We also present QMC data on the charge distribution of the host material around the impurity for the single-impurity case.

As expected, we will find that the quantitative results depend on the dimensionality and the band structure of the host material. In the following, we first show results for the 2D and 3D host materials with simple quadratic band dispersions. Then we discuss the case for a GaAs host using the tight binding approximation.

## 4.3 Two-Dimensional Case

In this section, we show results for the 2D case. Here, the density of states of the pure host, $\rho_0$, is a constant with a sharp cutoff at the semiconductor gap edge, which leads to stronger impurity–host coupling compared with the 3D case. Here, we present results for hybridization $\Delta \equiv \pi \rho_0 V^2$ varying from 1 to 4.

### 4.3.1 Magnetic Correlations Between the Impurities

Figures 4.2a–c show the impurity magnetic correlation function $\langle M_1^z M_2^z \rangle$ vs. $k_0 R$, where $R = |\mathbf{R}_1 - \mathbf{R}_2|$ is the impurity separation, at $\beta = 16$ for $\mu$ varying from $-6.0$ to 1.0. Figure 4.2a is for hybridization $\Delta = 1.0$. At $\mu = -6.0$, we observe oscillations in the $R$ dependence due to an RKKY-type effective interaction between the impurities. These results are similar to what has been obtained previously with QMC for a half-filled metallic band [11–13]. The wavelength of the oscillations increases when $\mu$ moves to $-1.0$, because of the shortening of the Fermi wavevector. When $\mu = 0.0$, the impurity spins exhibit long-range FM correlations at this temperature. We observe that upon further increasing $\mu$ to 0.5 or 1.0, the FM correlations become weaker. This is because the IBS becomes occupied as $\mu$ changes from 0.0 to 0.5, as will be seen in Fig. 4.3a. In Figs. 4.2b and c, results on $\langle M_1^z M_2^z \rangle$ are shown for $\Delta = 2.0$ and 4.0, respectively. In Fig. 4.2b, we observe that $\langle M_1^z M_2^z \rangle$ has the slowest decay for $\mu = 0.5$, while in Fig. 4.2c this occurs for $\mu = 1.0$. We find that the impurity occupation $\langle n_d \rangle$ increases between $\mu = 0.5$ and 1.0 for $\Delta = 2.0$ and $\beta = 16$. Hence, $0.5 < \omega_{\mathrm{IBS}} < 1.0$ for $\Delta = 2$. In addition, for $\Delta = 4.0$ and $\beta = 8$, the maximum-entropy image of $A(\omega)$ shows that the IBS is located

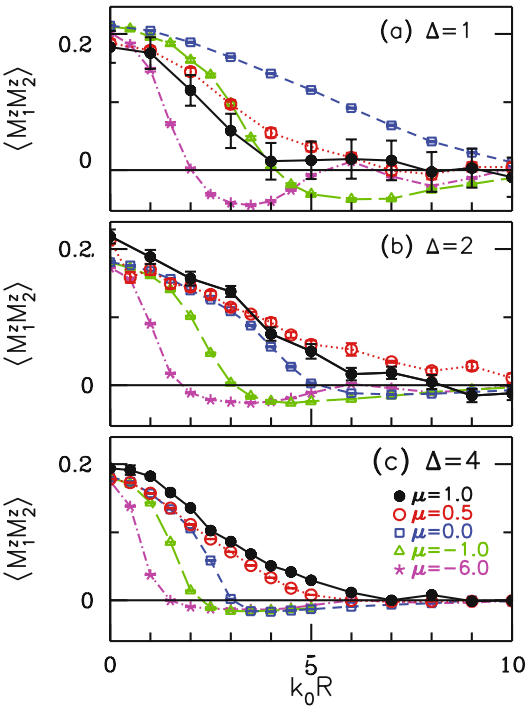


**Fig. 4.2.** $\langle M_1^z M_2^z \rangle$ vs. $k_0 R$ plotted at $\beta = 16$ and various $\mu$ for hybridization (**a**) $\Delta = 1.0$, (**b**) 2.0, and (**c**) 4.0

at $\omega \approx 1.0$. Hence, we observe that the range of the FM correlations for the semiconductor is determined by the occupation of the IBS in agreement with the HF predictions [5,6]. In Figs. 2a–c, it is also seen that the maximum range increases with decreasing $\Delta$.

In Fig. 4.3, we discuss the $\Delta = 1.0$ case in more detail. In Fig. 4.3a, the impurity spectral weight $A(\omega)$ vs. $\omega$ is plotted for $\beta = 8$, $\mu = 0.1$, and $k_0 R = 5$ and 10. Here, the $\omega$-axis has been shifted so that the top of the valence band is located at $\omega = 0$. For $k_0 R = 10$, we observe a peak at $\omega_{\rm BS} \approx 0.1$ in the semiconductor gap, which we identify as the IBS. For $k_0 R = 5$, the bound state is broader due to stronger correlations between the impurities. However, we also find that $A(\omega)$ exhibits significant $T$ dependence at $\beta = 8$, and Fig. 4.3a does not yet represent the low-$T$ limit. Next, in Figs. 4.3b and c, $\langle M_1^z M_2^z \rangle$ evaluated at $k_0 R = 5$ and 10 is plotted as a function of $\mu$. Figure 4.3b shows that, at low $T$ for $k_0 R = 5$, $\langle M_1^z M_2^z \rangle$ decreases when $\mu \gtrsim 0.25$. For this value of $k_0 R$ and $\beta = 32$, we find that the impurity occupation $\langle n_d \rangle$ develops a step discontinuity at $\mu \approx 0.25$, which is consistent with the decrease of $\langle M_1^z M_2^z \rangle$ when $\mu \gtrsim 0.25$. For $k_0 R = 10$ and $\beta = 32$, both $\langle M_1^z M_2^z \rangle$ and $\langle n_d \rangle$ exhibit significant $T$ dependence in the vicinity of the semiconductor gap edge. These results show that $\langle M_1^z M_2^z \rangle$ depends strongly on the value of $\mu$.

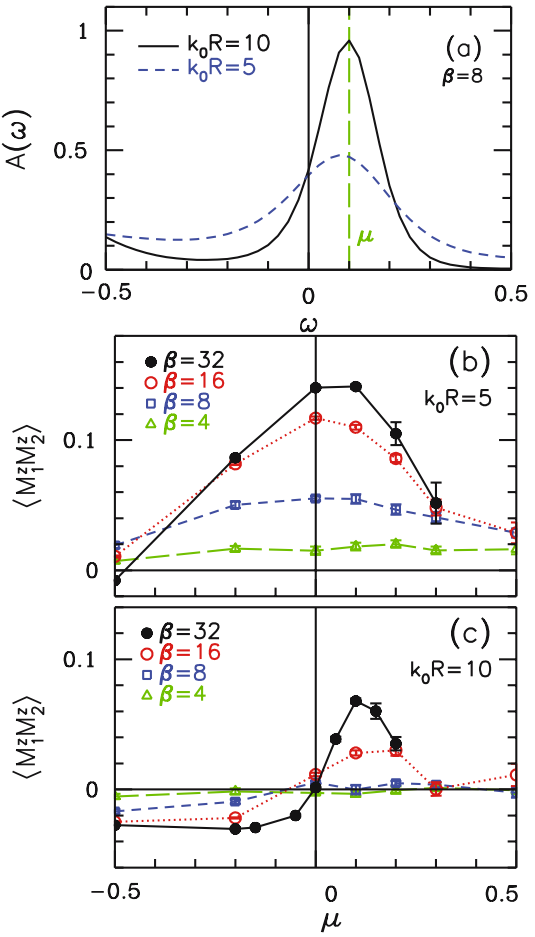


**Fig. 4.3.** (**a**) Impurity single-particle spectral weight $A(\omega)$ vs $\omega$ for $k_0R = 5$ and 10 at $\beta = 8$. Here, the *vertical dashed line* denotes $\mu$, and the top of the valence band is located at $\omega = 0$. In (**b**) and (**c**), $\langle M_1^z M_2^z \rangle$ vs $\mu$ is plotted for $k_0R = 5$ and 10, respectively, at various $\beta$. These results are for $\Delta = 1.0$

Figures 4.4a and b show $\langle M_1^z M_2^z \rangle$ vs. $k_0R$, where $R$ is the impurity separation, for the two-impurity Anderson model for half-filled metallic ($\mu = -6.0$) and semiconductor ($\mu = 0.1$) cases. On the one hand, in the metallic case, $\langle M_1^z M_2^z \rangle$ exhibits both FM and AFM correlations depending on the value of $k_0R$. On the other hand, for $\mu = 0.1$, we observe FM correlations of which range increases with $\beta$.

Figure 4.5 shows the inter-impurity magnetic susceptibility $\chi_{12}$ vs. the inverse temperature for various values of $\mu$ near the semiconductor gap edge. These results are for impurity separation $R = 10k_0^{-1}$. We observe that the FM correlations are strongest when $\mu$ is between the gap edge and the IBS.

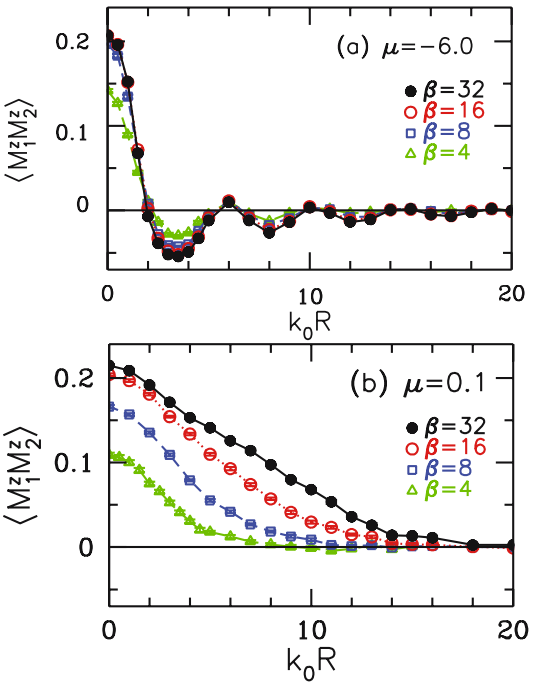


**Fig. 4.4.** Impurity-impurity magnetic correlation function $\langle M_1^z M_2^z \rangle$ vs $k_0 R$ at various $\beta$ for (**a**) $\mu = -6.0$ and (**b**) $\mu = 0.1$ for the two-impurity Anderson model

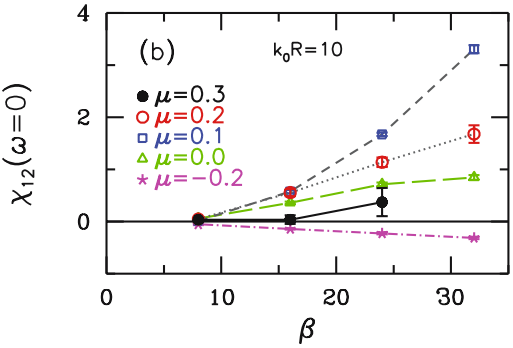


**Fig. 4.5.** Inter-impurity magnetic susceptibility $\chi_{12}(\omega = 0)$ vs $\beta$ for $k_0 R = 10$ at various $\mu$. These results are for $\Delta = 1.0$

The remainder of the data shown for the 2D case in this section are for the single-impurity Anderson model. In Fig. 4.6, we show results on $\langle (M^z)^2 \rangle$ vs. $\mu$ for various values of $\Delta$. As $T$ is lowered, a step discontinuity develops in $\langle (M^z)^2 \rangle$ near the gap edge. The location of the discontinuity coincides with the location of IBS deduced from data on $\langle M_1^z M_2^z \rangle$, $A(\omega)$, and $\chi_{12}$ discussed

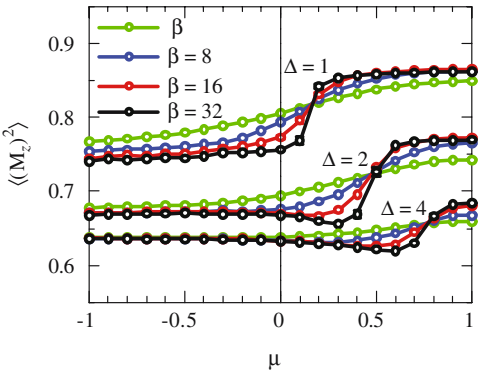


**Fig. 4.6.** Impurity magnetic moment square $\langle (M_z)^2 \rangle$ vs. $\mu$ at various $\beta$ for $\Delta = 1$, 2 and 4 for the single-impurity Anderson model

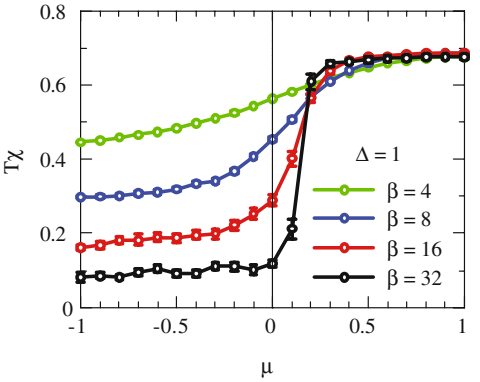


**Fig. 4.7.** $T\chi$ vs. $\mu$ at various $\beta$ for $\Delta = 1$ for the single-impurity Anderson model

above. Hence, Fig. 4.6 shows that the local moment increases rapidly as the IBS becomes occupied. Here, we also observe that the moment size decreases with increasing hybridization, as expected. Figure 4.7 shows $T\chi$ vs. $\mu$ for $\Delta = 1$, where we observe that a step discontinuity develops at the same location as in $\langle (M^z)^2 \rangle$ shown in Fig. 4.6a. For $\mu \lesssim \omega_{\rm IBS}$, $T\chi$ decreases with decreasing $T$ because of the screening of the impurity moment by the valence electrons. However, for $\mu \gtrsim \omega_{\rm IBS}$, the impurity susceptibility exhibits free-moment behavior in agreement with the role of the IBS discussed earlier. We note that determining the location of the IBS from $A(\omega)$ is costly in terms of computation time. For this reason, in the single-impurity case, it is more convenient to determine $\omega_{\rm IBS}$ from data on $\langle (M^z)^2 \rangle$ vs. $\mu$. In the remaining sections, we will use this approach for determining $\omega_{\rm IBS}$.

Finally, we note that within HF, $\omega_{\rm IBS} = 0.017$ for $\Delta = 1$. Hence, the HF approximation underestimates the value of $\omega_{\rm IBS}$ by about an order of

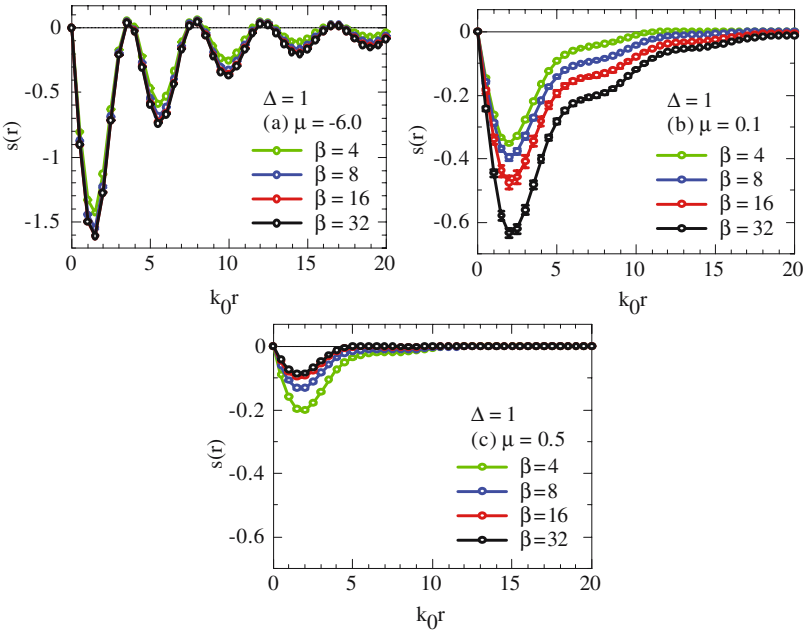


**Fig. 4.8.** Impurity–host magnetic correlation function $s(r)$ vs. $k_0 r$ at various $\beta$ for (**a**) $\mu = -6.0$, (**b**) $\mu = 0.1$, and (**c**) $\mu = 0.5$ for the single-impurity Anderson model

magnitude. Hence, for $\Delta = 1$, the long-range FM correlations would be restricted to a narrow range of $\mu$ within the HF approximation.

### 4.3.2 Impurity–Host Correlations

In this section, we discuss the magnetic correlations between the impurity and the host. In addition, we show results on the induced charge oscillations around the impurity site.

Figures 4.8a–c show the impurity–host magnetic correlation function $s(r)$ defined by

$$s(r) = \frac{2\pi k_0 r}{n_0} \langle M^z m^z(r) \rangle \tag{4.10}$$

vs. $k_0 r$ for the single-impurity Anderson model for $\mu = -6.0$ (half-filled metallic), $\mu = 0.1$ (semiconductor with IBS unoccupied), and $\mu = 0.5$ (semiconductor with IBS occupied). Here, $n_0$ is the electron density and $r$ is the distance from the impurity site. For $\mu = 0.1$, the coupling between the impurity and host spins is AFM for all values of $k_0 r$, while for $\mu = -6.0$, $s(r)$ exhibits RKKY-type $2k_F$ oscillations. We also note that, for the metallic case, the magnetic correlations saturate before reaching $\beta = 32$. Comparison of Fig. 4.8b and Fig. 4.4b for $\mu = 0.1$ show that the AFM impurity-host coupling produces the FM correlations between the impurities.

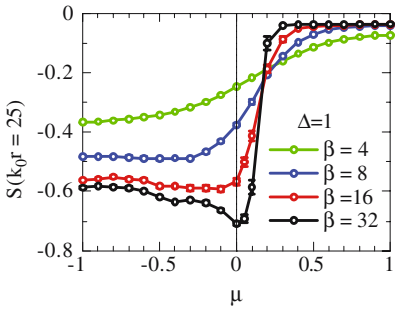


**Fig. 4.9.** $S(k_0 r = 25)$ vs. $\mu$ at various $\beta$ for the single-impurity Anderson model

As seen in Fig. 4.8c, when $\mu$ is increased to 0.5, the AFM correlations between the impurity and host spins become much weaker. This is because the IBS becomes occupied for $\mu > 0.1$. Within the HF approximation [5,6], the FM interaction between the impurities is mediated by the impurity-induced polarization of the valence electron spins, which exhibit an AFM coupling to the impurity moments. The impurity–host hybridization also induces host split-off states at the same energy as the IBS. When the split-off state becomes occupied, the spin polarizations of the valence band and the split-off state cancel. This causes the long-range FM correlations between the impurities to vanish. These QMC and HF results emphasize the role of the IBS in determining the range of the magnetic correlations for a semiconductor host.

The total magnetic coupling of the impurity magnetic moment to the host is obtained from

$$S(k_0 r) = \int_0^{k_0 r} d(k_0 r') s(r') \tag{4.11}$$

Figure 4.9 shows $S(k_0 r = 25)$ vs. $\mu$ for $\Delta = 1$ at various $\beta$. Here, we see that the impurity becomes magnetically decoupled from the host when $\mu \gtrsim \omega_{IBS}$.

Next, in Fig. 4.10, we show the modulation of the charge density around the impurity. Here, we plot $p(r)$ vs. $k_0 r$, where $p(r)$ is defined by

$$p(r) = \sum_{\alpha=v,c} \frac{2\pi k_0 r}{n_0} (n_\alpha(r) - n_\alpha(r = \infty)) \tag{4.12}$$

with $n_\alpha(r) = \sum_\sigma \langle c^\dagger_{\alpha\sigma}(r) c_{\alpha\sigma}(r) \rangle$. For the metallic case of $\mu = -6.0$, we observe long-range RKKY-type of oscillations in $p(r)$. When $\mu = 0.1$, the charge density around the impurity is depleted up to $k_0 R \approx 20$ at these temperatures. This depletion represents the extended valence hole, which forms around the impurity. However, for $\mu = 0.5$, the induced charge density decreases significantly as $T$ is lowered, because now the IBS is occupied. We next integrate $p(r)$,

$$P(k_0 r) = \int_0^{k_0 r} \mathrm{d}(k_0 r') p(r'), \tag{4.13}$$

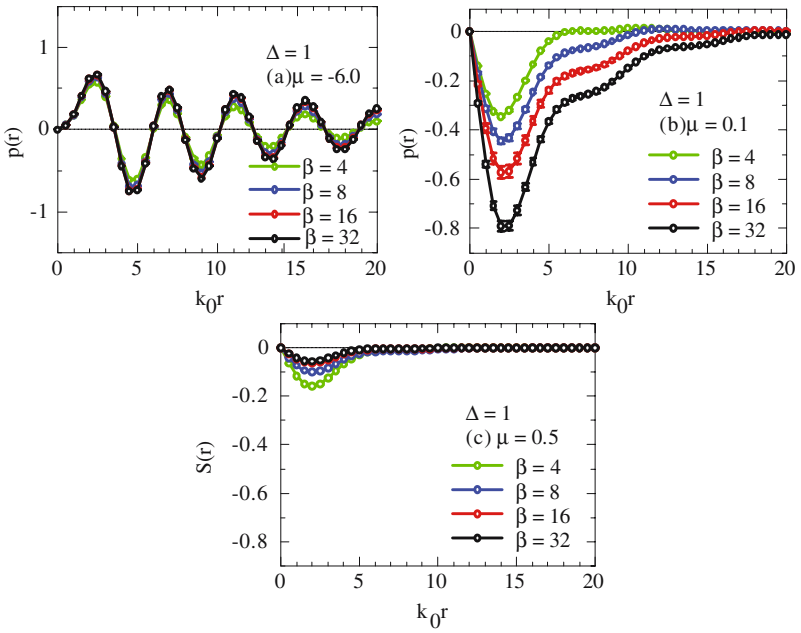


**Fig. 4.10.** $p(r)$ vs. $k_0 r$ for $\Delta = 1$ and (**a**) $\mu = -6.0$, (**b**) 0.1, and (**c**) 0.5

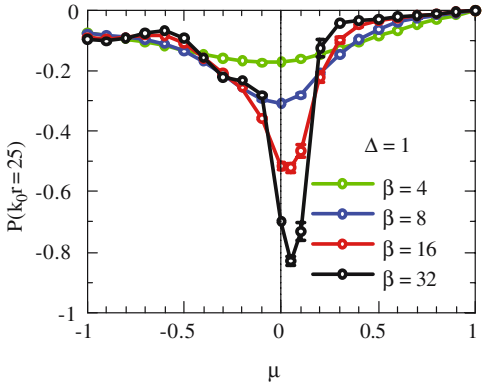


**Fig. 4.11.** $P(k_0 r = 25)$ vs. $\mu$ at various $\beta$ for the single-impurity Anderson model

and plot $P(k_0 r = 25)$ vs $\mu$ in Fig. 4.11. We observe that the total charge density around the impurity is most depleted when $0 \lesssim \mu \lesssim \omega_{\mathrm{IBS}}$, which is due to the valence hole induced around the impurity. In the metallic case, the induced charge density is oscillatory and has a long range as we have seen in Fig. 4.10a. As $\mu$ approaches the gap edge, the electron density around the impurity is depleted. However, when $\mu \gtrsim \omega_{IBS}$, we see that this depletion is canceled by the extended charge density of the split-off state.

## 4.4 Three-Dimensional Case

In this section, we discuss the 3D case, where the hybridization parameter $\pi V^2 N(0)$ vanishes at the gap edge because of the vanishing of $N(0)$ of the pure host. Hence, the impurity–host coupling near the gap edge is much weaker compared with the 2D case. Consequently, the FM correlations between the impurities have a shorter range. We find that the dimensionality of the host material strongly influences the magnetic correlations. In particular, we see that the IBS does not exist in 3D unless the hybridization is sufficiently large.

Here, we define hybridization as $\Delta = \pi\rho_0^* V^2$ where $\rho_0^*$ is the density of states when the valence band is half-filled, $\rho_0^* = k_0^3/(4\sqrt{2}\pi^2 D)$. This choice allows us to use comparable values for the hybridization matrix element $V$, when we compare the 2D and 3D results. In the following, we present results for $\Delta = 1$, 2, and 4.

Figures 4.12a–c show $\langle M_1^z M_2^z \rangle$ vs. $k_0 R$ at various values of $\mu$ for $\Delta = 1$, 2, and 4. These results are for $\mu = -6.0$, $\mu = -1.0$, and $\mu = 0.0$. On the one hand, we observe that, for $\Delta = 1$, the FM correlations between the impurities weaken as $\mu$ approaches the top of the valence band. On the other hand, for $\Delta = 2$ and 4, the FM correlations are stronger for $\mu = 0.0$. This is because, for $\Delta = 1$, the IBS does not exist in a 3D host, as we will see later in Fig. 4.15, which shows results on $\langle (M^z)^2 \rangle$ vs. $\mu$.

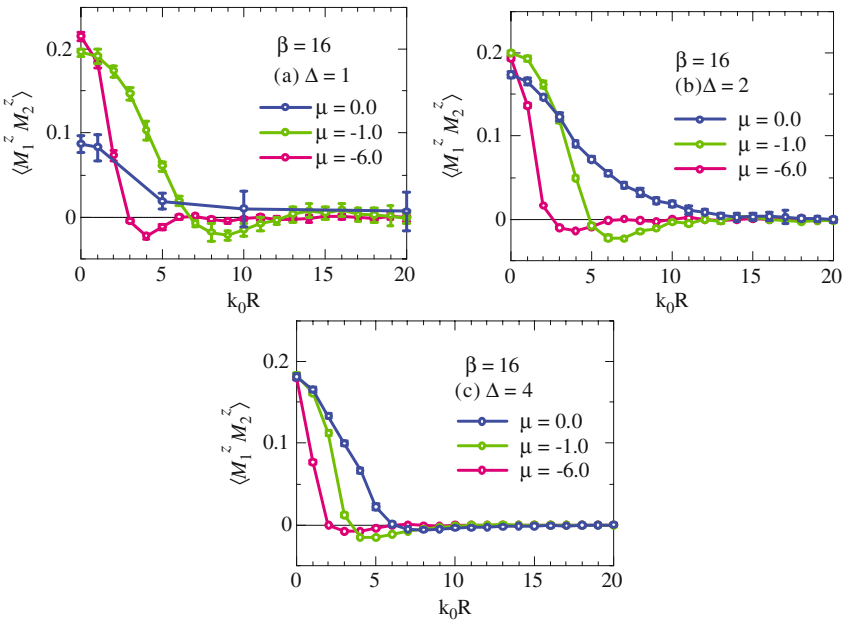


**Fig. 4.12.** $\langle M_1^z M_2^z \rangle$ vs. $k_0 R$ at $\beta = 16$ and various $\mu$ for hybridization (**a**) $\Delta = 1.0$, (**b**) 2.0, and (**c**) 4.0 in the 3D case

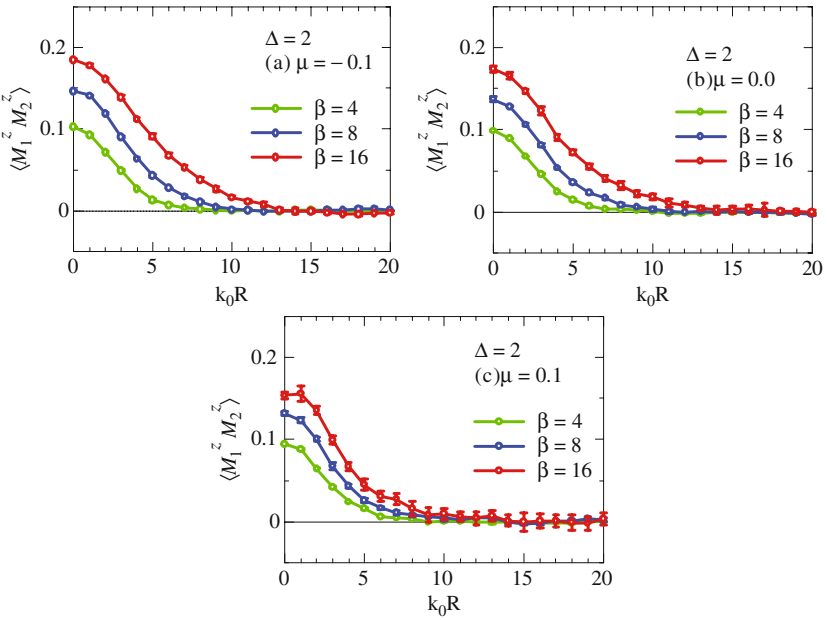


**Fig. 4.13.** $\langle M_1^z M_2^z \rangle$ vs. $k_0 R$ at various $\beta$ for $\Delta = 1$, and (**a**) $\mu = -0.1$, (**b**) $\mu = 0.0$, and (**c**) $\mu = 0.1$ in the 3D case

Next, in Fig. 4.13, we show $\langle M_1^z M_2^z \rangle$ vs. $k_0 R$ for $\Delta = 2$. We will see that for this value of $\Delta$, and IBS exists with $\omega_{\rm IBS} \approx 0.0$. Here results are shown at various values of $\beta$ for $\mu = -0.1$, 0.0 and 0.1. We observe that the FM correlations weaken as $\mu$ mover through $\mu = 0.0$.

Figure 4.14 shows the impurity-host magnetic correlation function $s(r)$ vs. $k_0 r$ for the single-impurity case for the same parameters as in Fig. 4.13. In 3D, $s(r)$ is defined by

$$s(r) = \frac{4\pi (k_0 r)^2}{n_0} \langle M^z m^z(r) \rangle. \tag{4.14}$$

We see that the impurity-host coupling weakens rapidly for $\mu \gtrsim 0.0$. These figures show that, in 3D and for $\Delta = 2$, the IBS is located at $\omega_{\rm IBS} \approx 0.0$, which is consistent with the results on $\langle (M^z)^2 \rangle$ shown in Fig. 4.15. In Fig. 4.15, for $\Delta = 1$, we do not observe the development of a discontinuity for temperatures down to $\beta = 32$. For $\Delta = 2$, we observe the development of a discontinuity centered at $\mu \approx 0.0$, as $\beta$ increases. For $\Delta = 4$, a step discontinuity at $\mu \approx 0.3$ is clearly observed. So, in 3D the IBS exists only for sufficiently large values of the hybridization matrix element $V$. This is consistent with the dependence of the IBS on the dimensionality in the $U = 0$ case. These results show that the dimensionality of the host material strongly influences the magnetic properties.

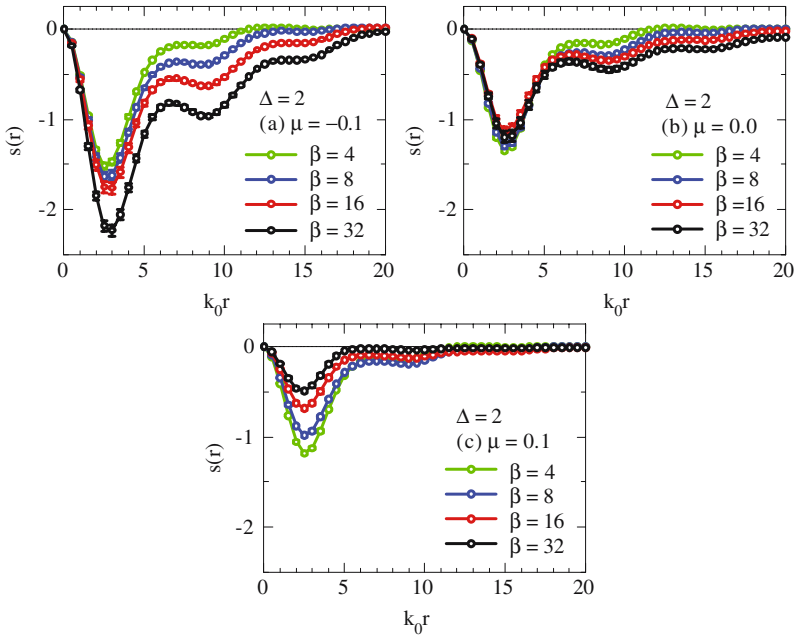


**Fig. 4.14.** $s(k_0 r)$ vs. $k_0 r$ at various $\beta$ for $\Delta = 2$ and for (**a**) $\mu = -0.1$, (**b**) 0.0, and (**c**) 0.1 for the single-impurity Anderson model in a 3D host

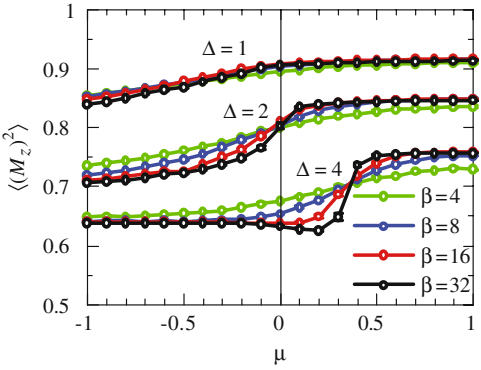


**Fig. 4.15.** Impurity magnetic moment square $\langle (M_z)^2 \rangle$ vs. $\mu$ at various $\beta$ for (**a**) $\Delta = 1$, 2, and 4 for the single-impurity Anderson model in a 3D host

The results presented in Sects. 4.3 and 4.4 show that the density of states of the pure host at the gap edge and the value of the hybridization matrix element are crucial in determining the magnetic properties when transition metal impurities are substituted into a semiconductor host. This means that the band structure of the pure host material will also be crucial in determining the magnetic properties. In the next section, we explore the consequences

of a more realistic band structure for a GaAs host using the tight-binding approximation.

## 4.5 Tight-Binding Model for a Mn *d* Orbital in GaAs

In this section, we study the magnetic correlations that develop when one $d_{xy}$ orbital is added to a GaAs host using the tight-binding approximation to calculate the host electronic structure and the host–impurity hybridization. Here, the tight-binding band structure of GaAs host is obtained by keeping the $s$ and the three $p$ orbitals at each site of the zincblende crystal structure of GaAs and by taking into account only the nearest-neighbor hoppings. We perform the QMC calculations for the case of a single Mn $d_{xy}$ orbital added to the GaAs host. Hence, we are assuming that the $sp^3$ orbitals of the Mn impurity are the same as those of Ga of the host material. We are also assuming that GaAs electronic structure is not modified by the additional $d$ orbital at the impurity site. In addition, here we consider only one of the three $t_{2g}$ orbitals of the Mn impurity, hence we neglect the spin-orbit interaction. Clearly, this is a simple model for a transition metal impurity substituted into GaAs. However, this approach allows us to take into account the effects of the host band structure beyond the quadratic dispersion used in the previous sections. Furthermore, in Sects. 4.3 and 4.4, we had treated the hybridization $\Delta$ as a free parameter. However, within this approach, we perform the calculations using realistic parameters for the hybridization of the $d$ orbital with the host.

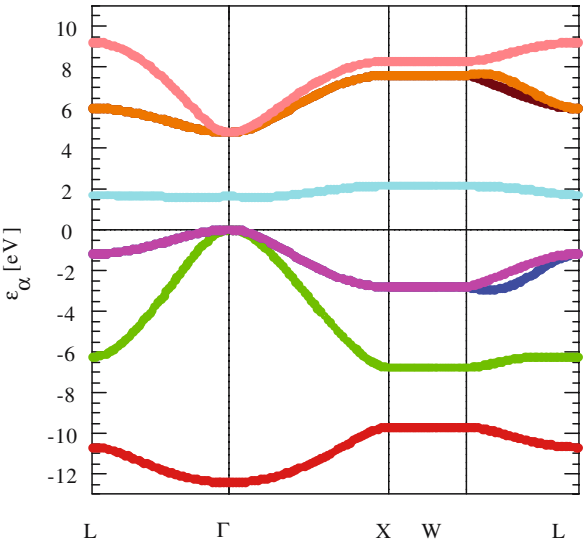


**Fig. 4.16.** Band structure of GaAs within the tight-binding approximation

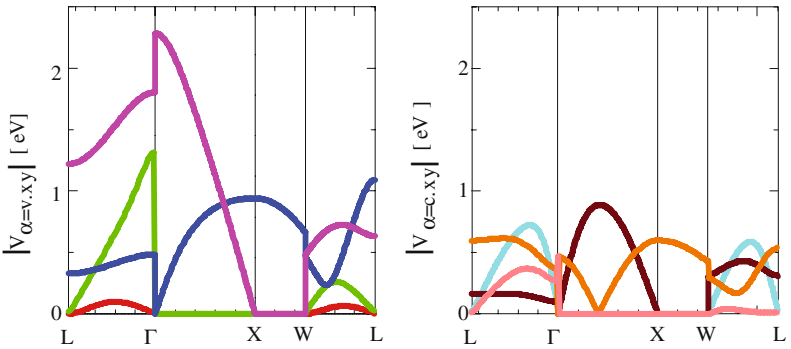


**Fig. 4.17.** Hybridization matrix element $V_{\alpha,xy}(\mathbf{k})$ of the $d_{xy}$ orbital of a Mn impurity with (**a**) the valence and (**b**) the conduction bands of GaAs vs. **k** obtained using the tight-binding approximation

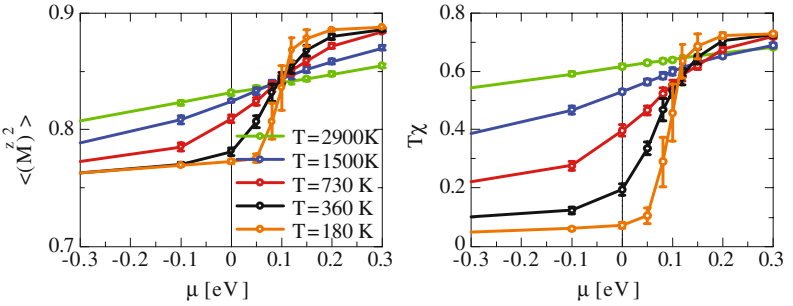


**Fig. 4.18.** (**a**) $\langle (M^z)^2 \rangle$ and (**b**) $T\chi$ vs. $\mu$ near the gap edge for a single $d_{xy}$ orbital added to the GaAs host

Figure 4.16 shows the tight-binding band structure of GaAs, which consists of eight bands originating from the $sp^3$ orbitals at each Ga and As site. Here, the bands $\varepsilon_\alpha(\mathbf{k})$ vs. **k** are plotted in the first Brillouin zone of the zincblende crystal structure. These bands were obtained by using the Slater-Koster parameters from Chadi and Cohen [16]. We note that the top of the valence band is located at the $\Gamma$ point, where the semiconductor gap is about $1.6\,eV$, consistent with the experimental value.

Next, Figs. 4.17a and b show the hybridization matrix element $V_{\alpha,xy}(\mathbf{k})$ of the $d_{xy}$ orbital with the valence and the conduction bands, respectively. In obtaining these results, we have taken the Slater-Koster parameter for $d-s$ hybridization, $c(ds)$, to be 0. We have also taken the ratio of the Slater-Koster parameters for the $d-p_\sigma$ hybridization to the $d-p_\pi$ hybridization, $c(dp_\sigma)/c(dp_\pi)$, to be $-2.16$ [17]. The results shown in Fig. 4.17 are for $c(dp_\sigma) = -1.1$ eV. The estimate for $c(dp_\sigma)$ from the photoemission experiments is $-1$ eV [18]. Hence, the tight-binding model parameters used in producing $\varepsilon_\alpha(\mathbf{k})$ and

$V_{\alpha,xy}(\mathbf{k})$ are reasonable. The values of $V_{\alpha,xy}(\mathbf{k})$ at the top of the valence and at the bottom of the conduction band will be particularly important for producing the IBS. Here, we observe that at the $\Gamma$ point, the impurity $d_{xy}$ orbital exhibits significant hybridization with the top of the valence point. However, the hybridization with the lowest-lying conduction band vanishes at the $\Gamma$ point.

Using the tight-binding results for $\varepsilon_\alpha(\mathbf{k})$ and $V_{\alpha,xy}(\mathbf{k})$ as input, we have performed the QMC simulations to study the magnetic properties. In Figs. 4.18a and b we show the resulting data on $\langle (M^z)^2 \rangle$ and $T\chi$ vs $\mu$. Here, we observe that a step discontinuity develops at $\omega_{IBS} \approx 100\,meV$, which is close to the experimental value of $110\,meV$ for dilute Mn impurities in GaAs [19]. We see that by using realistic parameters for the host band structure and the host–impurity hybridization, it is possible to obtain an accurate value for $\omega_{IBS}$. Such quantitative agreement supports the physical picture described in this chapter for the origin of the FM correlations in DMS.

## 4.6 Discussion and Summary

In the QMC and HF calculations, the location of the Fermi level with respect to the IBS is important; the FM correlations weaken as the IBS becomes occupied. Photoemission [20] and optical measurements [21] on $Ga_{1-x}Mn_xAs$ suggested the existence of an IBS above the top of the valence band in this prototypical DMS ferromagnet. Photoemission experiments [20] observed an Mn-induced state above the valence band and right below the Fermi level in $Ga_{1-x}Mn_xAs$. Clearly, inverse photoemission experiments are required to detect the unoccupied portion of the Mn-induced impurity band. STM experiments also observed the impurity band in this compound [22]. The transport measurements [23] on insulating samples of (Ga,Mn)As with less than 1% Mn impurities also suggest the existence of an IBS in the semiconductor gap. However, in metallic samples with more than 2% Mn, no activated contribution from an IBS to dc transport has been observed. We think that the physical picture presented in this chapter is consistent with the experiments in (Ga,Mn)As in the dilute impurity limit, and provides a mechanism for the origin of ferromagnetism. In particular, by using the tight-binding results for the host electronic structure and the impurity–host hybridization as input for the QMC calculations, we have obtained $\omega_{\mathrm{IBS}} \approx 100\,meV$, which is close to the experimental value. These comparisons suggest that the Anderson Hamiltonian for a semiconductor host provides a basic electronic model for the DMS ferromagnets.

Alternative ways of enhancing the FM correlations in this model is provided by varying the hybridization parameter $\Delta$ or the semiconductor gap $\Delta_G$. The QMC simulations show that $\xi$ increases as $\Delta$ goes from 4.0 to 1.0. Within HF, $\xi$ can take very large values as $\Delta/\Delta_G$ decreases. Hence, new DMS compounds with weaker hybridization or a larger semiconductor gap might lead

to higher Curie temperatures. However, it is necessary to keep in mind that the two-impurity Anderson model for a semiconductor host might be oversimplified for describing the ferromagnetism of the DMS. Our calculations are for spin-1/2 Anderson impurities, and we have neglected the multiorbital structure of the spin-5/2 Mn impurities. We are currently performing calculations for the multiorbital case, which take into account the Hund's rule coupling between the three Mn $t_{2g}$ orbitals.

Various other theoretical approaches have been used to describe the ferromagnetism of DMS and to predict the Curie temperature as a function of the Mn concentration. These include the coherent potential approximation (CPA) and LDA+$U$ techniques, which describe the host band structure accurately but treat the Coulomb correlations at mean-field level [24]. In particular, we note that the CPA or LDA+$U$ type calculations cannot be relied upon to accurately predict the dependence of the FM correlations on $\mu$ or $\Delta/\Delta_G$. In this respect, the results presented in this chapter are valuable because here the many-body effects due to the Coulomb correlations at the impurity site in a semiconductor host have been treated exactly. For example, we have observed that, within the HF approximation, the long-range FM correlations are restricted to a narrow range of $\mu$. We also point out that the dependence of the Curie temperature on the carrier concentration has been studied for DMS using a disordered RKKY model [25]. However, our results show that the RKKY form is not appropriate for describing the interimpurity magnetic correlations when the host is a semiconductor.

Recently, $T_c$'s exceeding the room temperature have been reported in dilute oxides such as ZnO and $TiO_2$ with transition metal impurities [26, 27]. The importance of the oxygen vacancies in producing the ferromagnetism has been pointed out experimentally [28]. Perturbative and LSDA+$U$ mean-field calculations have been performed to describe the ferromagnetism induced by oxygen vacancies in (Ti,Co)$O_2$ [29, 30]. We think that it would also be useful to perform exact numerical calculations to study the role of the vacancy band in producing the FM correlations in this compound.

In summary, we have presented QMC results to show that long-range FM correlations develop between magnetic impurities in semiconductors. In particular, the FM correlations have the longest range when the Fermi level is located above the top of the valence band, and they weaken as the IBS becomes occupied. Hence, the position of the Fermi level with respect to the IBS plays a crucial role in determining the range of the FM correlations in qualitative agreement with HF. These results also show that the RKKY form is not appropriate for describing the inter-impurity magnetic correlations when the host is a semiconductor. Finally, comparisons with the experimental data suggest that the Anderson model for a semiconductor host captures the basic electronic structure of the DMS ferromagnets.

**Acknowledgment**

This work was supported by the NAREGI Nanoscience Project and a Grant-in Aid for Scientific Research from the Ministry of Education, Culture, Sports, Science and Technology of Japan, and NEDO.

## References

1. *Concepts in Spin Electronics*, edited by S. Maekawa (Oxford Univ. Press, 2006).
2. H. Ohno, H. Munekata, T. Penney, S. von Molnar, L.L. Chang, Phys. Rev. Lett. **68**, 2664 (1992); H. Ohno, A. Shen, F. Matsukura, A. Oiwa, A. End, S. Katsumoto, Y. Iye, Appl. Phys. Lett. **69**, 363 (1996)
3. I. Žutić, J. Fabian, S. Das Sarma, Rev. Mod. Phys. **76**, 323 (2004)
4. F.D.M. Haldane, P.W. Anderson, Phys. Rev. B **13**, 2553 (1976)
5. M. Ichimura, K. Tanikawa, S. Takahashi, G. Baskaran, S. Maekawa, in *Foundations of Quantum Mechanics in the Light of New Technology* (ISOM-Tokyo 2005), ed. by S. Ishioka, K. Fujikawa, (World Scientific, Singapore, 2006), pp. 183–186, (cond-mat/0701736)
6. K. Tanikawa, S. Takahashi, M. Ichimura, G. Baskaran, S. Maekawa, unpublished
7. P.M. Krstajić, V.A. Ivanov, F.M. Peeters, V. Fleurov, K. Kikoin, Europhys. Lett. **61**, 235 (2003)
8. K. Yamauchi, H. Maebashi, H. Katayama-Yoshida, J. Phys. Soc. Jpn. **72**, 2029 (2003)
9. J. Inoue, S. Nonoyama, H. Itoh, Phys. Rev. Lett. **85**, 4610 (2000)
10. N. Bulut, K. Tanikawa, S. Takahashi, S. Maekawa, Phys. Rev. B **76**, 045220 (2007)
11. J.E. Hirsch, R.M. Fye, Phys. Rev. Lett. **56**, 2521 (1986)
12. R.M. Fye, J.E. Hirsch, Phys. Rev. B **38**, 433 (1988)
13. R.M. Fye, J.E. Hirsch, D.J. Scalapino, Phys. Rev. B **35**, 4901 (1987)
14. J.E. Gubernatis, J.E. Hirsch, D.J. Scalapino, Phys. Rev. B **35**, 8478 (1987)
15. W. von der Linden, Appl. Phys. A **60**, 155 (1995)
16. D.J. Chadi, M.L. Cohen, Phys. Stat. Sol. (b) **68**, 405 (1975)
17. W.A. Harrison, *Electronic Structure and the Properties of Solids* (Dover, New York, 1989)
18. T. Mizokawa, private communication
19. J.S. Blakemore, W.J. Brown, M.L. Stass, D.D. Woodbury, J. App. Phys. **44**, 3352 (1973)
20. J. Okabayashi, A. Kimura, O. Rader, T. Mizokawa, A. Fujimori, T. Hayashi, M. Tanaka, Phys. Rev. B **64**, 125304 (2001)
21. K.S. Burch, D.B. Shrekenhamer, E.J. Singley, J. Stephens, B.L. Sheu, R.K. Kawakami, P. Schiffer, N. Samarth, D.D. Awschalom, D.N. Basov, Phys. Rev. Lett. **97**, 087208 (2006)
22. A.M. Yakunin, A.Yu. Silov, P.M. Koenraad, J.H. Wolter, W. Van Roy, J. De Boeck, J.-M. Tang, M.E. Flatte, Phys. Rev. Lett. **92**, 216806 (2004)
23. T. Jungwirth et al., Phys. Rev. B **76**, 125206 (2007)
24. T. Jungwirth, J. Sinova, J. Masek, J. Kucera, A.H. MacDonald, Rev. Mod. Phys. **78**, 809 (2006)
25. D.J. Priour, S. Das Sarma, Phys. Rev. Lett. **97**, 127201 (2006)

26. Y. Matsumoto, M. Murakami, T. Shono, T. Hasegawa, T. Fukumura, M. Kawasaki, P. Ahmet, T. Chikyow, S. Koshihara, H. Koinuma, Science **291**, 854 (2001)
27. P. Sharma, A. Gupta, K.V. Rao, F.J. Owens, R. Sharma, R. Ahuja, J.M.O. Guillen, B. Johansson, G.A. Gehring, Nature Mater. **2**, 673 (2003)
28. K.A. Griffin, A.B. Pakhomov, C.M. Wang, S.M. Heald, K.M. Krishnan, Phys. Rev. Lett. **94**, 157204 (2005)
29. K. Kikoin, V. Fleurov, Phys. Rev. B **74**, 174407 (2006)
30. V.I. Anisimov et al., J. Phys. Cond. Mat. **18**, 1695 (2006)